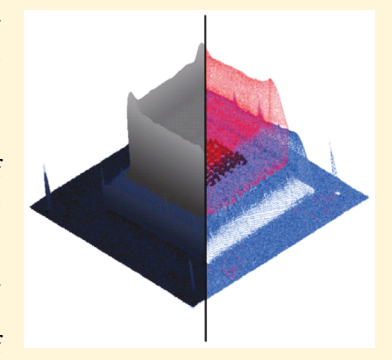


New Algorithm to Enable Construction and Display of 3D Structures from Scanning Probe Microscopy Images Acquired Layer-by-Layer

William Nanqiao Deng,^{‡,§} Shuo Wang,^{†,§} Joao Ventrici de Souza,[†] Tonya L. Kuhl,[‡] and Gang-yu Liu^{*,†}®

ABSTRACT: Scanning probe microscopy (SPM), such as atomic force microscopy (AFM), is widely known for high-resolution imaging of surface structures and nanolithography in two dimensions (2D), providing important physical insights into surface science and material science. This work reports a new algorithm to enable construction and display of layer-by-layer 3D structures from SPM images. The algorithm enables alignment of SPM images acquired during layer-by-layer deposition and removal of redundant features and faithfully constructs the deposited 3D structures. The display uses a "see-through" strategy to enable the structure of each layer to be visible. The results demonstrate high spatial accuracy as well as algorithm versatility; users can set parameters for reconstruction and display as per image quality and research needs. To the best of our knowledge, this method represents the first report to enable SPM technology for 3D imaging construction and display. The detailed algorithm is provided to facilitate usage of the same approach in any SPM software. These new capabilities support wide applications



of SPM that require 3D image reconstruction and display, such as 3D nanoprinting and 3D additive and subtractive

1. INTRODUCTION

manufacturing and imaging.

Scanning probe microscopy (SPM), such as atomic force microscopy (AFM), is well-known for its high spatial resolution ability, 1-5 imaging in various media in real time, 6-9 and enabling of nanolithography. 10-14 These capabilities provide much new physical insight into surface chemistry, materials science, and biological science. 15-1 Despite these advantages, SPM exhibits the limitation of being a 2D imaging and lithography technology. Recent advances increase the demands in construction of 3D structures from layer-by-layer AFM topographic images. The needs come from SPM-based 3D nanolithography, which produces 3D structures with designed feature sizes at nanometer precision, ^{24–26} as well as additive ^{27–29} and subtractive ³⁰ imaging and manufacturing. In current SPM technology, researchers attain 3D structural information by displaying all 2D topographic images, e.g., 10 AFM topographic images in the case of a 10-layered structure. Researchers need to visualize each 2D image and mentally stack these layers in order to imagine the corresponding 3D structures, often cumbersome and difficult, especially when there are numerous layers. Moreover, the construction of 3D structures from a series of 2D AFM topographical images is challenging and unlike that of other technologies. For example, laser scanning confocal microscopy (LSCM) acquires a series of fluorescence images slice-by-slice and then simply stacks these slices to attain the 3D images. 31-34 3D printers could do the same. However, neither the software nor the algorithms can be applied to SPM images because of two primary reasons. First, redundancy in AFM images; the images are not slices at

various z levels but instead are surface contours of the outermost shell of the entire region acquired frame-by-frame. Second, misalignment from image to image: SPM probes feature molecular or nanometer precision, and as such, it is difficult to maintain identical regions from scan to scan. 35-38 Such shifts or "misalignments" are neither apparent nor significant in lower-resolution imaging techniques but become problematic in SPM. This work reports a new algorithm that aligns images by using landmarks (engineered or naturally present) and affine transformation. Although affine transformation has been widely applied for image registration, 39-43 our work represents the first time that this approach is applied to high-resolution SPM images. Redundant data points are removed by using an algorithm developed by us called Sweeping. The program can also provide a "see-through" display to enable the structure in each layer to be visible in one image. Using actual structures and images from our own AFM 3D nanoprinting process, this work demonstrates the high spatial accuracy as well as the versatility of this algorithm. AFM users could add this algorithm as part of their data acquisition and analysis software and set their own parameters for reconstruction and display as per image quality and research needs. The new capabilities enhance SPM technology by supporting applications that require 3D image reconstruction and display, such as 3D nanoprinting and 3D additive and subtractive imaging and manufacturing.

Received: April 10, 2018 Revised: June 1, 2018 Published: June 11, 2018



[†]Department of Chemistry, University of California, Davis, California 95616, United States

^{*}Department of Chemical Engineering, University of California, Davis, California 95616, United States

The Journal of Physical Chemistry A

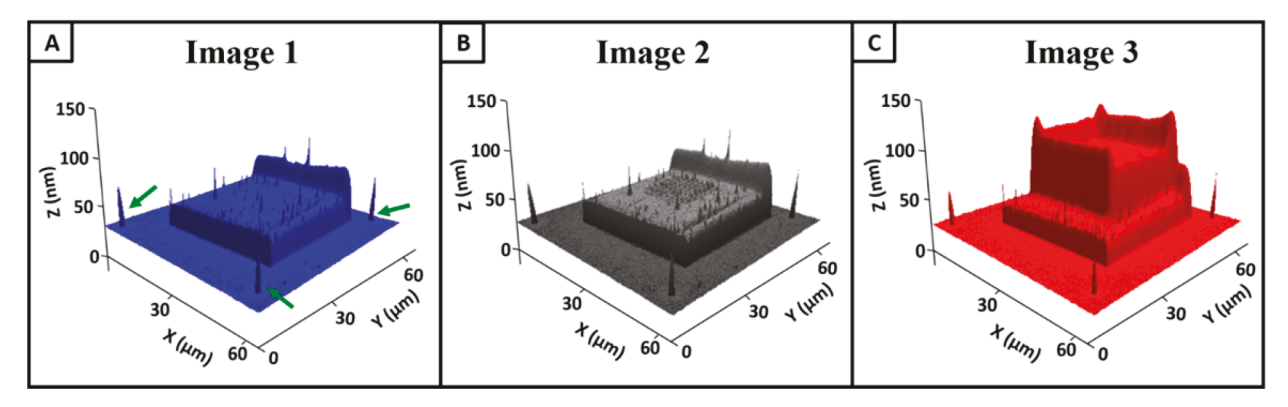


Figure 1. AFM topographic images acquired after printing the first (A), second (B), and third (C) layer, respectively. The three landmarks are indicated by green arrows in (A). A 65 μ m × 65 μ m area was scanned at a 50.01 μ m/s speed and 1024 × 1024 line density under tapping mode in an ambient environment.

2. EXPERIMENTAL SECTION

2.1. Materials and Supplies. The following reagents were used as received: Sulfuric acid (95.0–98.0%) and hydrogen peroxide (30% aqueous solution) were purchased from EMD Chemicals (Gibbstown, NJ, U.S.A.). Deionized and ultrapure water (18.2 M Ω ·cm at 25 °C) was obtained from a Milli-Q water system (EMD Millipore, Billerica, MA, U.S.A.). Nitrogen gas (99.999%) was purchased from Praxair, Inc. (Danbury, CT, U.S.A.). Loctite AA 349 (Henkel, Germany) consists of a mixture of methacrylate esters, which polymerize upon exposure to UV radiation (~365 nm).

Surfaces used for this investigation were 1 × 3 in.² glass slides (Fisherfinest Premium, Fisher Scientific, Pittsburgh, PA, U.S.A.), which were subject to standard glassware cleaning: 2 h of immersion in Piranha solution, consisting of 3 parts of sulfuric acid to 1 part of hydrogen peroxide (30% aq.). These pretreated glass slides were copiously rinsed with Milli-Q water and finally dried under a flow of nitrogen for 5 min.

2.2. 3D Nanoprinting Using an AFM-Based Nanofluidic Device. The 3D structures used for this work were designed using FluidFM ARYA operator software. The printing process was carried out under ambient conditions and followed previously established protocols developed by our team.²⁵ Briefly here, an integrated AFM and microfluidic platform, FluidFM BOT (Cytosurge, Glattbrugg, Switzerland), enabled 3D printing. The system also contained an inverted optical microscope (IX-73, Olympus America, Center Valley, PA, U.S.A.). The printing was carried out with a FluidFM nanopipette (CYPR/001511, Cytosurge, Glattbrugg, Switzerland) with a 300 nm opening at the end of its microchannel. The delivery was controlled by varying the probe-surface contact time, the probe-surface contact force, and liquid pressure from -800 to +1000 mbar with 1 mbar precision. Hamilton 7000 series syringes, 1 μ L (Hamilton, Reno, NV, U.S.A.), were used to preload materials into a 2 μ L reservoir behind the micropipette. Most 0D features, e.g., mounds of the photopolymerizable polymer, were printed under a typical contact force of 45 nN, pressure of 200 mbar, and a dwell time of 5 s, while 1D features required continuous contact at a speed of 20 μ m/s under 200 mbar. Cuboid features were printed line-by-line with an interline separation approximately equal to the line width. After printing each layer, the sample was illuminated under a high-intensity long-wave (~365 nm) UV radiation (UV lamp Model B-100A, Ted Pella, Inc., Redding, CA, U.S.A.) for 5 min to allow photopolymerization

or curing. The deposited structures were then characterized via AFM imaging (see the next section) before printing additional layers.

2.3. High-Resolution Layer-by-Layer Imaging Using AFM. Topographic, amplitude, and phase images were acquired after printing of each layer using a deflection type AFM (MFP-3D, Oxford Instrument, Santa Barbara, CA, U.S.A.). All AFM images were acquired under tapping mode in ambient conditions. Probes (AC240-TS, Olympus America, Central Valley, PA, U.S.A.) with a typical spring constant of 1.7 N/m and resonant frequency of 57 kHz were used for high-resolution imaging.

The driving frequency was set at the fundamental resonance of the cantilever, and the driving amplitude was typically 1 V with 40% damping, while topographic, amplitude, and phase images were acquired at the same time. For this work, only topographic images were used to illustrate our concepts. Image acquisition and simple processing were performed on the MFP-3D software developed on the Igor Pro 6.20 platform.

3. RESULTS AND DISCUSSION

3.1. Design, Production, and Layer-by-Layer AFM Imaging of 3D Structures. Simple three-layer structures with designed geometry and dimensions of photopolymers are used to illustrate our algorithm. The printing follows our AFM-based 3D nanolithography protocols reported previously. The results of AFM imaging after each printing step are shown in Figure 1. To facilitate the initial development of the algorithm, we printed three cone-shaped features located at the three corners of the image frame during the first printing, as shown in Figure 1A. Each cone measures 50 ± 3 nm tall with a full width at half-maximum (FWHM) of $2.3 \pm 0.3~\mu m$.

These features serve as landmarks toward the development and testing of our new algorithm. The central feature was a 40 $\mu m \times$ 40 $\mu m \times$ 30 nm cuboid. The far side edge of the cuboid was printed taller (60 nm) than the rest by pulsing at the edge during printing. This design ensures that the orientation of the central cuboid can be clearly determined regardless of how the images undergo rotations and alignment procedures during algorithm development. The cuboid was printed line-by-line, with each being about 40 μm long and 130 lines in total.

The second layer was printed atop the first. The design consisted of 9 \times 9 crossing grids with 2 μ m separation. As shown in Figure 1B, these crossing grids were 4 nm tall. The third layer was a 30 μ m \times 30 μ m \times 50 nm cuboid with turrets.

The Journal of Physical Chemistry A

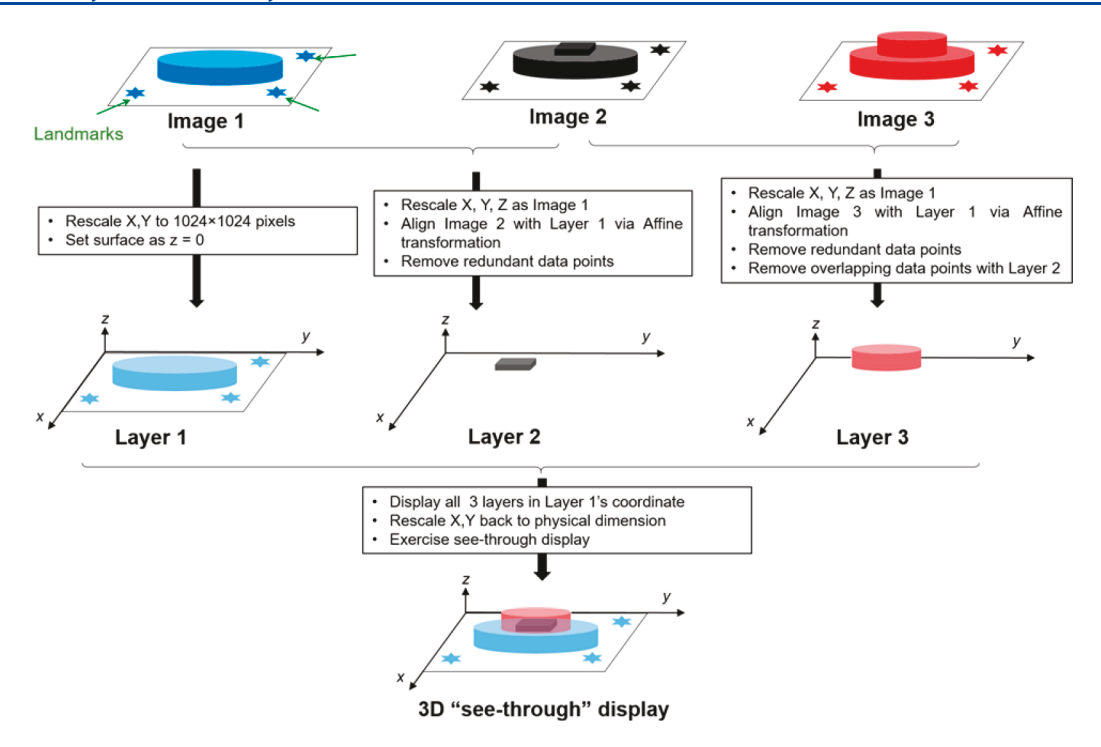


Figure 2. Schematic diagram illustrating the reconstruction and display of 3D structures from AFM images acquired in sequence.

The turret had three walls and three parapets at the corners. The walls measured 23 \pm 3 nm in height and 2.3 \pm 0.2 μ m in width. The three parapets measured 12 ± 2 nm in height above the wall. The FWHMs of the parapets were 2.6, 3.1, and 3.5 μ m moving clockwise. As can be seen from Figure 1C, all three landmarks retained their structural integrity throughout the entire experiment. All three AFM images shown in Figure 1 were acquired under identical imaging conditions. Most commercial AFM data acquisition and display software enables various means to display images, e.g., 2D, 3D, with numerous choices of orientation, color, and shade. For visual clarity, all AFM images shown in Figure 1 were flattened and displayed in the same orientation and scale. Clearly, all grids (2nd layer) and a portion of the base cuboid (1st layer) were "buried" and not visible in the final AFM image (Figure 1C). Therefore, one needs to have all three images on display in order to mentally reconstruct and visualize the genuine 3D structure. The following section will introduce the new algorithm to enable reconstruction of the 3D structures from AFM images acquired layer-by-layer, and the final image enables visualization of the 3D structure including intricate internal features. The minimum number of layers required for proof-of-concept is three, thus the example shown in Figure 1. Current SPM lithography enables production of 3D nanostructures by design up to 10s of layers, as demonstrated by us and other researchers, 24-26,44,45 which could incorporate the algorithm by simply adding iterations for additional layers.

3.2. Key Steps in the Algorithm. The key steps and principles of our algorithm are shown in Figure 2 using a three-layered structure as an example. The same concepts are applicable to additional numbers of layers following the same treatment as Layer 3. Landmarks must be identified—either artificially printed (Figure 2) or by selecting three or more distinct structural features. AFM topographic images taken after each layer are referred to as Image 1, 2, and 3, respectively. For accurate alignment, the algorithm first

converts the AFM topographic images by rescaling X, Y into pixel coordinates, e.g., 1024×1024 . This conversion equalizes the resolution of the first and later layers regardless of the initial imaging conditions, e.g. the first layer was acquired at 256×256 lines, while the second image was 512×512 lines. The algorithm then sets the surface as z = 0 by first taking the average z value from flat surface regions (nonlandmark and nonfeatured areas) and then defining the average z value as zero. Finally, Image 1 is converted and displayed in the new coordinate, e.g., 1024 pixels \times 1024 pixels \times 160 nm, referred to as "Layer 1". Image 2 is aligned with Layer 1 through two main steps: (a) z is aligned following the same algorithm to set the surface as z = 0; (b) the lateral alignment is accomplished by first pixelating the x, y values and then superposing the three landmarks and the two coordinates with Layer 1 via affine transformation (see details in section 3.4). Image 2 at this stage is converted into Image 2*, i.e., aligned and displayed in the same coordinate as Layer 1. Finally, Layer 2 is generated by removing redundant data points (those already in Layer 1) from Image 2*. Layer 3 and subsequent layers are generated by following protocols similar to those of Layer 2, using Layer 1's coordinate for alignment, and then removing redundant data points (already in Layer 1 and 2) from Image 3*. As a final step, all of the layers are displayed in the same coordinate of Layer 1, and the x, y pixel coordinates are converted back to the physical dimensions. The see-through display is achieved by using a single pixel to display each data point and lowering the color density of each layer to allow transparency.

3.3. Generation of Layer 1. As illustrated in Figure 2, the original AFM image, shown in Figure 1A, was first rescaled by converting X, Y coordinates into pixels without altering the z values. The concept can be realized using any AFM software. Our algorithm uses Igor Pro 6.0 to enable compatibility and integration into this commonly used data acquisition software. First, the X and Y values in the original AFM data were stored as Igor Pro binary wave (.ibw) files and assigned as 0-1023

pixels by doing a direct data transfer from the .ibw format to an Igor 2D wave. The indices of the new wave represent the location of the pixels, and physical dimension data is removed for alignment purpose.

Next, the z values of the surface region (areas surrounding the landmark and central features) were averaged mathematically, and the averaged value $\langle z \rangle$ was set to 0. This step places the surface of Layer 1 at the XY plane (z = 0). In the case of Figure 1A where a flat surface was used as a printing canvas, a flat area in the surface region, e.g., 200 × 400 pixels, would be sufficient to represent the entire surface. To avoid the impact of random and sharp spikes due to noise, contamination, or tall surface features above the base surface, z values larger than one standard deviation were excluded from the mean value calculation. This window can be set higher or lower based on the actual surface roughness and signal/noise (S/N) of the individual images. Upon determining the average value, $\langle z \rangle$, the z value of Image 1 was set to $z_{\text{new}} = z - \langle z \rangle$, e.g., moving the entire image downward along the z axis by the distance of $\langle z \rangle$ in the case that $\langle z \rangle$ is a positive value. The outcome, Layer 1, is displayed in Figure 3B. In order to fulfill the requirement

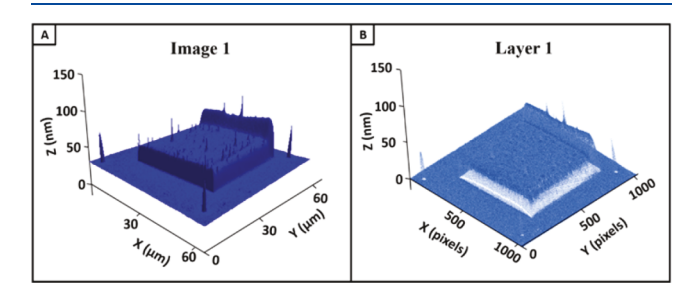


Figure 3. Comparison of (A) original Image 1 with (B) Layer 1 generated from (A) using our algorithm.

of true 3D and see-through, two display settings were also exercised: (a) each point in Layer 1 was displayed as a single pixel and (b) a transparency factor, α value of 0.5, was assigned to each pixel to lower the color intensity in Figure 3B. The α values could range from 0 (completely transparent) to 1 (completely opaque), as per the user's preference and data's needs. For comparison, the original AFM image is displayed in Figure 3A, so that one can see the differences in the X and Y axes, z values, and transparency. As in conventional AFM image display, Figure 3A uses a solid square for each point to present a solid appearance. In contrast, Figure 3B not only reveals the geometry of Layer 1, it also allows transparency by displaying the layer in meshes.

3.4. Generation of Layer 2. As illustrated in Figure 2 (middle), Image 2 (Figure 1B) is first rescaled following the same algorithm as used for Image 1. The rescaled Image 2 is referred to as Image 2', whose X and Y axes are pixelated, with the surface as z=0. Next, Image 2' is aligned with Layer 1. As discussed in the Introduction, it is common in AFM imaging that one frame shifts from another due to drift. For example, the three landmarks in Image 1, although physically the same, may have different X, Y, Z values from that of Image 2 due to lateral, vertical, and/or rotational drift. In some cases, drift may be severe enough that one cannot completely superposition the two images via lateral and vertical movement alone. To ensure alignment at the nanometer scale and to merge and unify the coordinates, affine transformation is employed.

Using the alignment and coordinate unification of Layer 1 and Image 2' as an example, two main steps are required in the algorithm: (a) a 3×2 matrix, consisting of six elements, used in affine transformation is determined by aligning the three landmarks in the two images, and (b) the two images are transformed into the same coordinate as that in Layer 1. In principle, one needs a minimum of six equations to solve for the six elements in the 3×2 matrix. The three landmarks provide a more than sufficient number of data points for this exercise. Using the highest point in each landmark, as an example, the XY values in Image 2' and Layer 1 follow simple linear algebra in eq 1, where the three points in Layer 1 are (X_{1a}, Y_{1a}) , (X_{1b}, Y_{1b}) , and (X_{1c}, Y_{1c}) , respectively, and the three points from Image 2' are $(X_{2a'}, Y_{2a'})$, $(X_{2b'}, Y_{2b'})$, and $(X_{2c'}, Y_{2b'})$ $Y_{2c'}$), respectively. Solving the six linear equations in eq 1 allowed the determination of all elements in the 3×2 matrix. We note that the algorithm allows more data points from landmarks to be used to determine the matrix elements, although the three points used in eq 1 were used to illustrate the concept.

$$\begin{bmatrix} X_{2a'} \\ Y_{2a'} \end{bmatrix} = \begin{bmatrix} a_{11} & a_{12} & a_{13} \\ a_{21} & a_{22} & a_{23} \end{bmatrix} \begin{bmatrix} X_{1a} \\ Y_{1a} \\ 1 \end{bmatrix} \\
\begin{bmatrix} X_{2b'} \\ Y_{2b'} \end{bmatrix} = \begin{bmatrix} a_{11} & a_{12} & a_{13} \\ a_{21} & a_{22} & a_{23} \end{bmatrix} \begin{bmatrix} X_{1b} \\ Y_{1b} \\ 1 \end{bmatrix} \\
\begin{bmatrix} X_{2c'} \\ Y_{2c'} \end{bmatrix} = \begin{bmatrix} a_{11} & a_{12} & a_{13} \\ a_{21} & a_{22} & a_{23} \end{bmatrix} \begin{bmatrix} X_{1c} \\ Y_{1c} \\ 1 \end{bmatrix}$$
(1)

With the transformation matrix determined, the algorithm applies this 3×2 matrix to Layer 1, i.e., affine transformation, as shown in eq 2. This exercise transforms the numeric data of Layer 1 into Layer 1^s, which shares the same coordinate as Image 2', with all three landmarks aligned.

$$\begin{bmatrix} X_{1s} \\ Y_{1s} \end{bmatrix} = \begin{bmatrix} a_{11} & a_{12} & a_{13} \\ a_{21} & a_{22} & a_{23} \end{bmatrix} \begin{bmatrix} X_{1} \\ Y_{1} \\ 1 \end{bmatrix}$$
(2)

Upon completion of alignment and unification of coordinates, the final task is to remove out-of-range (points outside of the lateral range of Layer 1) and redundant data points (those already in Layer 1) from Image 2', yielding Layer 2, i.e., sharing the same coordinate as Layer 1 and containing only features printed in the second layer. This task is accomplished using Sweeping. Two key steps follow. First, out-of-range data points from Image 2' are removed and placed in the coordinate of Layer 1. Simply take each point in Layer 1s, (X_{1s}, Y_{1s}, Z_{1s}) , and check for a data point in Image 2' $(X_{2'}, Y_{2'}, Z_{2'})$ with the same X, Y values, i.e., $X_{1s} = X_{2'}$ and $Y_{1s} = Y_{2'}$. If true, a data point is entered into a new image file, Image 2*, as $(X_1, Y_1, Z_{2'})$. In other words, the X, Y values of Layer 1 corresponding to this point are entered, along with the Z value from Image 2'. If not true, the point will not be entered in Image 2*. In that case, data points that are outside of the lateral range of Layer 1 are all effectively removed. By applying this algorithm, Image 2*

The Journal of Physical Chemistry A

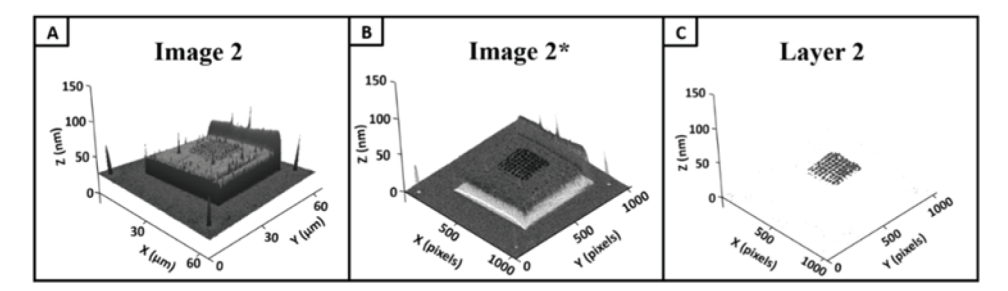


Figure 4. Comparison of (A) Image 2 with (B) Image 2* and (C) Layer 2. Image 2* is generated from Image 2 and Layer 1, while Layer 2 is generated from Image 2* and Layer 1 using our algorithm.

(Figure 4B) is generated, which has all out-of-range data points removed, aligned, and unified into the coordinate of Layer 1.

Second, overlapping points with Layer 1 are removed from Image 2* to generate Layer 2. This step is the most challenging due to the nature of AFM technology. From a mathematics prospective, Layer 2 can be easily generated by removing data points in Image 2* that are identical to those of Layer 1. However, one will soon find that there will be no identical points because even the same structural feature, upon coordinate unification, often exhibits different z values from one scan to another. This arises from the high spatial resolution/requirements of SPM in contrast to other imaging technology, i.e,. each pixel may only probe molecular- to nanometer-sized regions, and therefore, it is nearly impossible to hit the identical point from image to image. Our algorithm deals with this complication by introducing two heuristic parameters to allow probing data points in the local vicinity. The first parameter, k_1 (0-0.5) defines a local XY range centralized around selected data points in Layer 1. The relative differences in Z values at these points are compared to determine if the Z values are deemed equal as set by the cutoff parameter k_2 (0-100%), i.e., smaller k_2 , more strict requirements in Z values. Taking one data point from Image 2^* , (X_{2^*}) Y_{2*} , Z_{2*}), for example, the algorithm first encloses a range of data points centralized around this selected point. If $k_1 = 0.004$, then the XY ranges are 1024×0.004 pixels, and the enclosure would contain ±4 pixels in lateral directions centralized around (X_{2*}, Y_{2*}) , i.e., 64 data points. Then, the algorithm locates the corresponding central point in Layer 1, (X_1, Y_1, Z_1) , where X_1 = X_{2*} , Y_1 = Y_{2*} . Next, the algorithm calculates the relative Zvalue difference (%) of all 64 data points in Image 2* with that in Layer 1 and compares with k_2 . If all 64 points satisfy $|Z_{2*}|$ $Z_1 | / Z_{2*} \ge k_2$, the central point from Image 2*, (X_{2*}, Y_{2*}, Z_{2*}) , will be considered a "true new structural feature" from printing and become a new data point in Layer 2. If unsatisfied, the central point, (X_{2*}, Y_{2*}, Z_{2*}) , of Image 2* will be considered an "identical point with Layer 1" and therefore be removed. This exercise of fuzziness successfully enables the definition of "identical data points" and removal of redundant data from Image 2^* . Optimal k_1 and k_2 values are based on imaging resolution and conditions. Upon completion of all data points in Image 2*, Layer 2 will be generated. In our case, Layer 2 (shown in Figure 4C) was generated with $k_1 = 0.004$ and $k_2 =$ 5%. Only cross-grids printed in the second deposition remained, while all structural features in Layer 1 were removed. As seen from Figure 4, Layer 2 was much thinner than Layer 1 and thus easily overshadowed. This exercise enables clear visualization of Layer 2 only. In addition, this exercise would also enable researchers to clearly determine if interlayer interactions would occur, such as chemical reactions between Layer 2 and Layer 1.

3.5. Generation of Layer 3. As illustrated in Figure 2, the *X*, *Y*, *Z* axes of Image 3 are first rescaled following the same algorithm as that used with Image 1. Then, the rescaled Image 3 is aligned with Layer 1, and the out-of-range points are removed following the same protocols as those in section 3.4 to generate Image 3*, whose coordinate is now identical to those of Layer 1 and Layer 2. Finally, Layer 3 (shown in Figure 5C) is generated by extracting pure structural features due to

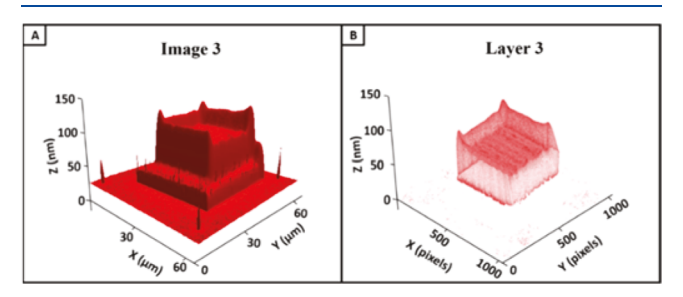


Figure 5. Comparison of (A) Image 3 and (B) Layer 3 generated from Image 3 and Layers 1 and 2 via our algorithm.

printing of the third cuboid. First, the redundant data points of Layer 1 are removed from Image 3^* following the same algorithm as that discussed in the last paragraph in section 3.4. Then, the overlapping data points with Layer 2 are also removed following the same algorithm as that in the last paragraph of section 3.4. For both actions, k_1 and k_2 are set to 0.004 and 5%, respectively. Additional layers in more complex 3D structures can be handled in an identical manner.

3.6. 3D See-Through Display. Because all three layers are aligned and in the same coordinate, the construction and display of the 3D and internal structure are simply achieved by placing all three layers in one coordinate. The X and Y axes is then converted back to the physical dimension, 65 μ m × 65 μ m, in reverse to the step described in the first paragraph of section 3.3. Finally, each layer is assigned a chosen color or grayscale and transparency, e.g., blue, black, and red for Layer 1, 2, and 3, respectively, at $\alpha = 0.5$. As can be seen from the outcome, Figure 6A, the geometries of the 3D structures are displayed accurately and clearly. The grid features in Layer 2 are now clearly visible, in contrast to Figure 1C where the Layer 2 is completely buried under Layer 3. In addition, our algorithm also supports grayscale display, as shown in Figure 6B, which has as good of quality as Figure 6A. One only needs to display this one image instead of multiple images from all layers to reveal the 3D structures qualitatively and quantitatively. To the best of our knowledge, this is the first

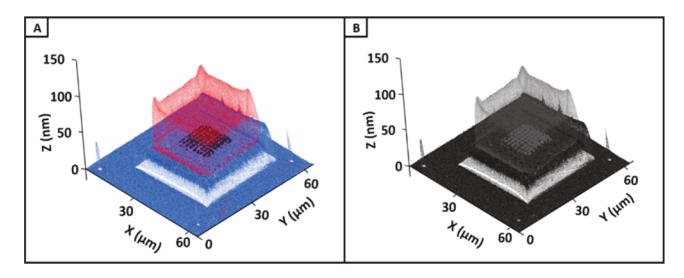


Figure 6. See-through display of the 3D structures constructed from AFM images: (A) with tricolors, each representing a layer; (B) with grayscale, each shade representing a layer.

report where 3D structures are constructed and displayed layer-by-layer from AFM topographic images. This see-through display is particularly powerful in the context of 3D nanoprinting because interlayer registry is enabled from nearest-neighbor layer to all layers. For example, one could design the fourth layer in desired registry with the first not just the third layer.

3.7. Robustness and Versatility of the Algorithm. To test the robustness and flexibility of the algorithm, we cropped images shown in Figure 1 to the central 50 μ m \times 50 μ m area, thus excluding all three landmarks. In the absence of engineered landmarks, one must select repeating natural features from all images to serve as landmarks. These features must remain throughout the printing process without being "buried" or altered in later processes. In the case of our 3D structures, we selected three features, circled in Figure 7A, to serve as the new landmarks. These three peaks were also clearly visible and remained unchanged in Images 2 and 3, as shown in Figure 7B,C.

The final display is shown in Figure 7D after running the algorithm without any changes in the code. The generated display is almost identical to the case when three engineered landmarks were used, as shown in Figure 6A, this display having the same good quality in displaying each layer's features. Each layer is clearly represented by one single color, and no mixture of colors was observed, which demonstrates that the alignment of AFM images was achieved with high spatial accuracy. Multiple sets of 3D structures with various designs were also tested using the algorithm. Among all tests, the algorithm reached lateral and vertical alignment up to 34 and 0.5 nm accuracy, respectively. The overall and internal structural details are clearly visualized in the final display. This test demonstrates the accuracy and flexibility of our algorithm to accommodate research needs in 3D printing, landmark selection, and image analysis.

For 3D structures with more than three layers, the algorithm can be run with additional iterations. We have tested a variety of 3D structures with up to nine layers, and each layer is still clearly visible in the final display. To ensure clear display, we recommend that colors with high contrast be assigned to adjacent layers to make each layer distinguishable, e.g., blue vs orange. The actual transparency is created through a combination of displaying the layer as pixelated points and use of Alpha blending. As the α value increases, the density of the color increases, which reduces transparency. In most AFM images, features become faint with α < 0.2 and nearly opaque when $\alpha > 0.8$. Thus, users could adjust the α value to achieve their display goals. We recommend the internal layer's α value be higher than the outer layers to allow visualization of the inter layers. This algorithm is coded using Igor Pro 6.20, adopted by current commercial SPM manufacturers. It is already integrated in the current AFM data acquisition and analysis software, MFP-3D Igor Pro 6.20. The detailed algorithm was reported to facilitate use of the same approach for other SPM software platforms.

4. CONCLUSIONS

This work reports a new algorithm to enable construction and display of 3D structures from SPM images acquired layer-bylayer. The algorithm addresses two key challenges in 3D image construction in SPM: (a) redundancy in AFM images and (b) misalignment from image to image. The algorithm aligns images by using landmarks (engineered or naturally present) and affine transformation. The redundant data points are removed by our developed algorithm, Sweeping. The seethrough display enables the overall and internal structures to be visible in one image. Using our own AFM-based 3D fabrication technology, layer-by-layer 3D structures were fabricated, and the corresponding AFM images were acquired. With the new algorithm, the AFM images were reconstructed and the 3D structures were displayed with each layer marked in high spatial accuracy. This new algorithm enhances SPM technology by supporting applications that require 3D image reconstruction and display, including 3D nanoprinting. subtractive and additive lithography and imaging, and detecting and revealing interlayer interactions. AFM users could add this algorithm as a part of their data acquisition and analysis software with parameters for reconstruction and display as per image quality and research needs. Work is in progress to support additional data analysis, e.g., cursor options and display options to make it more user-friendly.

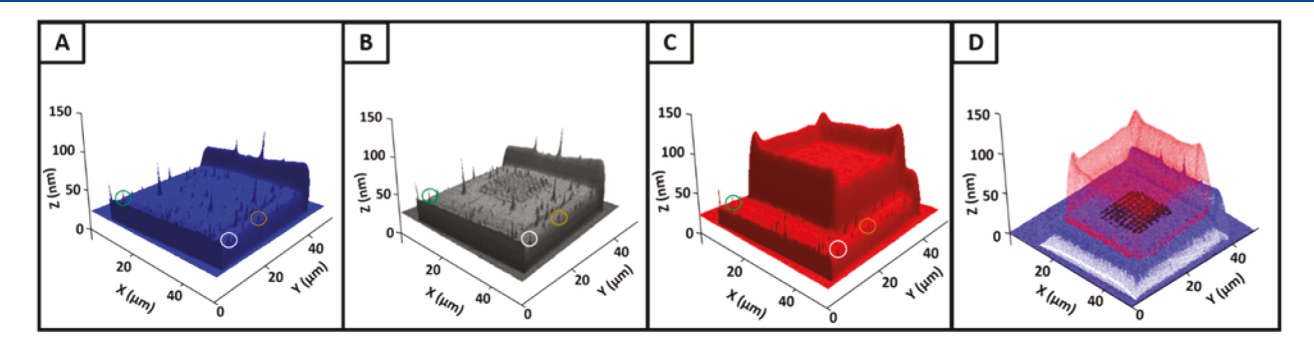


Figure 7. (A–C) The same AFM images cropped from Figure 1A–C, respectively. The three features (a spike within each circle) are selected to serve as landmarks to test the algorithm. (D) Final see-through display of the constructed 3D structures.

AUTHOR INFORMATION

Corresponding Author

*E-mail: gyliu@ucdavis.edu. Phone: (530) 754-9678. Fax: (530) 754-8557.

ORCID

Gang-yu Liu: 0000-0003-3689-0685

Author Contributions

§W.N.D. and S.W. made equal contributions to this work.

Notes

The authors declare no competing financial interest.

ACKNOWLEDGMENTS

We gratefully acknowledge support from the Gordon and Betty Moore Foundation and the National Science Foundation (CHE-1413708 and 1808829). J.V.d.S. received a graduate fellowship from the Brazilian National Council for Scientific and Technological Development (CNPq).

REFERENCES

- (1) Ohnesorge, F.; Binnig, G. True atomic resolution by atomic force microscopy through repulsive and attractive forces. *Science* **1993**, 260, 1451–1456.
- (2) Bottomley, L. A.; Coury, J. E.; First, P. N. Scanning probe microscopy. *Anal. Chem.* **1996**, *68*, 185–230.
- (3) Binnig, G.; Quate, C. F.; Gerber, C. Atomic force microscope. *Phys. Rev. Lett.* **1986**, 56, 930–933.
- (4) Radmacher, M.; Tillamnn, R.; Fritz, M.; Gaub, H. From molecules to cells: imaging soft samples with the atomic force microscope. *Science* **1992**, *257*, 1900–1905.
- (5) Engel, A.; Schoenenberger, C.-A.; Müller, D. J. High resolution imaging of native biological sample surfaces using scanning probe microscopy. *Curr. Opin. Struct. Biol.* 1997, 7, 279–284.
- (6) Xu, S.; Cruchon-Dupeyrat, S. J.; Garno, J. C.; Liu, G.-Y.; Kane Jennings, G.; Yong, T.-H.; Laibinis, P. E. In situ studies of thiol self-assembly on gold from solution using atomic force microscopy. *J. Chem. Phys.* **1998**, *108*, 5002–5012.
- (7) Milosavljević, N. B.; Ristić, M. Đ.; Perić-Grujić, A. A.; Filipović, J. M.; Štrbac, S. B.; Rakočević, Z. L.; Krušić, M. T. K. Removal of Cu2+ ions using hydrogels of chitosan, itaconic and methacrylic acid: FTIR, SEM/EDX, AFM, kinetic and equilibrium study. *Colloids Surf.*, A 2011, 388, 59–69.
- (8) Schelling, C.; Springholz, G.; Schäffler, F. Kinetic growth instabilities on vicinal Si (001) surfaces. *Phys. Rev. Lett.* **1999**, 83 (5), 995–998.
- (9) Rastelli, A.; Stoffel, M.; Tersoff, J.; Kar, G.; Schmidt, O. Kinetic evolution and equilibrium morphology of strained islands. *Phys. Rev. Lett.* **2005**, 95 (2), 026103.
- (10) Braunschweig, A. B.; Huo, F.; Mirkin, C. A. Molecular printing. *Nat. Chem.* **2009**, *1*, 353–358.
- (11) Ginger, D. S.; Zhang, H.; Mirkin, C. A. The evolution of dip-Pen nanolithography. *Angew. Chem., Int. Ed.* **2004**, 43, 30–45.
- (12) Liu, M.; Amro, N. A.; Liu, G.-y. Nanografting for surface physical chemistry. *Annu. Rev. Phys. Chem.* **2008**, *59*, 367–386.
- (13) Garcia, R.; Knoll, A. W.; Riedo, E. Advanced scanning probe lithography. *Nat. Nanotechnol.* **2014**, *9*, 577–587.
- (14) Radha, B.; Liu, G.; Eichelsdoerfer, D. J.; Kulkarni, G. U.; Mirkin, C. A. Layer-by-layer assembly of a metallomesogen by dip-pen nanolithography. *ACS Nano* **2013**, *7*, 2602–2609.
- (15) Alessandrini, A.; Muscatello, U. AFM and FTIR spectroscopy investigation of the inverted hexagonal phase of cardiolipin. *J. Phys. Chem. B* **2009**, *113*, 3437–3444.
- (16) Berg, F.; Wilken, J.; Helm, C. A.; Block, S. AFM-based quantification of conformational changes in DNA caused by reactive oxygen species. *J. Phys. Chem. B* **2015**, *119*, 25–32.

- (17) Hassan, N.; Maldonado-Valderrama, J.; Gunning, A. P.; Morris, V. J.; Ruso, J. M. Surface characterization and AFM imaging of mixed fibrinogen—surfactant films. *J. Phys. Chem. B* **2011**, *115*, 6304–6311.
- (18) İto, Y.; Hara, Y.; Uetsuka, H.; Hasuda, H.; Onishi, H.; Arakawa, H.; Ikai, A.; Yoshida, R. AFM observation of immobilized self-oscillating polymer. *J. Phys. Chem. B* **2006**, *110*, 5170–5173.
- (19) Rozhok, S.; Sun, P.; Piner, R.; Lieberman, M.; Mirkin, C. A. AFM study of water meniscus formation between an AFM tip and NaCl substrate. *J. Phys. Chem. B* **2004**, *108*, 7814–7819.
- (20) Calò, A.; Domingo, N.; Santos, S.; Verdaguer, A. Revealing water films structure from force reconstruction in dynamic AFM. *J. Phys. Chem. C* **2015**, *119*, 8258–8265.
- (21) Hinaut, A.; Lekhal, K.; Aivazian, G.; Bataillé, S.; Gourdon, A.; Martrou, D.; Gauthier, S. NC-AFM study of the adsorption of hexamethoxytriphenylene on KBr(001). *J. Phys. Chem. C* **2011**, *115*, 13338–13342.
- (22) Wang, M.; Yang, Y.-L.; Deng, K.; Wang, C. Uncoiling process of helical molecular fibrillar structures studied by AFM. *J. Phys. Chem. C* **2007**, *111*, 6194–6198.
- (23) Zhang, H.; Müllen, K.; De Feyter, S. Pulsed-force-mode AFM studies of polyphenylene dendrimers on self-assembled monolayers. *J. Phys. Chem. C* **2007**, *111*, 8142–8144.
- (24) Zhao, J. L.; Swartz, L. A.; Lin, W. F.; Schlenoff, P. S.; Frommer, J.; Schlenoff, J. B.; Liu, G. Y. Three-dimensional nanoprinting via scanning probe lithography-delivered layer-by-layer deposition. *ACS Nano* **2016**, *10*, 5656–5662.
- (25) Ventrici de Souza, J.; Liu, Y.; Wang, S.; Dorig, P.; Kuhl, T. L.; Frommer, J.; Liu, G. Y. Three-dimensional nanoprinting via direct delivery. *J. Phys. Chem. B* **2018**, *122*, 956–962.
- (26) Hirt, L.; Ihle, S.; Pan, Z. J.; Dorwling-Carter, L.; Reiser, A.; Wheeler, J. M.; Spolenak, R.; Voros, J.; Zambelli, T. Template-free 3d microprinting of metals using a force-controlled nanopipette for layer-by-layer electrodeposition. *Adv. Mater.* **2016**, 28, 2311–2315.
- (27) Radha, B.; Liu, G. L.; Eichelsdoerfer, D. J.; Kulkarni, G. U.; Mirkin, C. A. Layer-by-layer assembly of a metallomesogen by dip-pen nanolithography. *ACS Nano* **2013**, *7*, 2602–2609.
- (28) Drexler, C. I.; Moore, K. B., III; Causey, C. P.; Mullen, T. J. Atomic force microscopy characterization and lithography of culigated mercaptoalkanoic acid "Molecular Ruler" multilayers. *Langmuir* **2014**, *30*, 7447–7455.
- (29) Pires, D.; Hedrick, J. L.; De Silva, A.; Frommer, J.; Gotsmann, B.; Wolf, H.; Despont, M.; Duerig, U.; Knoll, A. W. Nanoscale three-dimensional patterning of molecular resists by scanning probes. *Science* **2010**, 328, 732–735.
- (30) Liu, J.-F.; Cruchon-Dupeyrat, S.; Garno, J. C.; Frommer, J.; Liu, G.-Y. Three-dimensional nanostructure construction via nanografting: Positive and negative pattern transfer. *Nano Lett.* **2002**, *2*, 937–940.
- (31) Kubinova, L.; Janacek, J.; Antos, K.; Jezek, B.; Indra, M.; Jirak, D.; Krekule, I. Application of graphical workstation SGI INDY and IBM PC to rendering and visualization of the objects captured by a confocal microscope. *Acta Vet. Brno* **1996**, *65*, 253–262.
- (32) Ramesh, N.; Otsuna, H.; Tasdizen, T. *Three-dimentional alignment and merging of confocal microscopy stacks*. 20th IEEE International Conference on Image Processing, Melbourne, VIC, 2013; pp 1447–1450.
- (33) Berthing, T.; Bonde, S.; Rostgaard, K. R.; Madsen, M. H.; Sorensen, C. B.; Nygard, J.; Martinez, K. L. Cell membrane conformation at vertical nanowire array interface revealed by fluorescence imaging. *Nanotechnology* **2012**, *23* (41), 415102.
- (34) Elgharably, H.; Mann, E.; Awad, H.; Gordillo, G.; Roy, S.; Sai-Sudhakar, C. B.; Wozniak, D. J.; Sen, C. K.; et al. First evidence of sternal wound biofilm following cardiac surgery. *PLoS One* **2013**, *8*, e70360
- (35) Lapshin, R. V. Feature-oriented scanning methodology for probe microscopy and nanotechnology. *Nanotechnology* **2004**, *15*, 1135–1151.
- (36) Lapshin, R. V. Automatic drift elimination in probe microscope images based on techniques of counter-scanning and topography feature recognition. *Meas. Sci. Technol.* **2007**, *18*, 907–927.

- (37) Yurov, V. Y.; Klimov, A. N. Scanning tunneling microscope calibration and reconstruction of real image drift and slope elimination. *Rev. Sci. Instrum.* **1994**, *65*, 1551–1557.
- (38) Zhang, L. S.; Long, Q.; Liu, Y. B.; Zhang, J.; Feng, Z. H. Correlation-steered scanning for scanning probe microscopes to overcome thermal drift for ultra-long time scanning. *Ultramicroscopy* **2016**, *166*, 16–26.
- (39) Yang, F.; Deng, Z. S.; Fan, Q. H. A method for fast automated microscope image stitching. *Micron* **2013**, *48*, 17–25.
- (40) Song, Z. L.; Zhou, S. G.; Guan, J. H. A novel image registration algorithm for remote sensing under affine transformation. *IEEE Trans. Geosci. Electron* **2014**, *52*, 4895–4912.
- (41) Gong, M. G.; Zhao, S. M.; Jiao, L. C.; Tian, D. Y.; Wang, S. A novel coarse-to-fine scheme for automatic image registration based on SIFT and mutual information. *IEEE Trans. Geosci. Electron* **2014**, *52*, 4328–4338.
- (42) Zitova, B.; Flusser, J. Image registration methods: A survey. *Image and Vision Computing* **2003**, 21, 977–1000.
- (43) Fernandes, L. A. F.; Oliveira, M. M. Geometric algebra: A powerful tool for solving geometric problems in visual computing. Tutorials of the XXII Brazilian symposium on cumputer graphics and image processing 2009, 17–30.
- (44) Gruter, R. R.; Voros, J.; Zambelli, T. FluidFM as a lithography tool in liquid: spatially controlled deposition of fluorescent nanoparticles. *Nanoscale* **2013**, *5*, 1097–1104.
- (45) Meister, A.; Gabi, M.; Behr, P.; Studer, P.; Voros, J.; Niedermann, P.; Bitterli, J.; Polesel-Maris, J.; Liley, M.; Heinzelmann, H.; et al. FluidFM: Combining atomic force microscopy and nanofluidics in a universal liquid delivery system for single cell applications and beyond. *Nano Lett.* **2009**, *9*, 2501–2507.
- (46) Porter, T.; Duff, T. Compositing Digital Images. Computer Graphics 1984, 18, 253–259.
- (47) Wallace, B. Merging and transformation of raster images for carton animation. *Computer Graphics* **1981**, *15*, 253–262.